RSC Advances

PAPER

View Article Online
View Journal | View Issue



Cite this: *RSC Adv.*, 2024, **14**, 38035

# Effect of a self-assembled 3D flower-like hierarchical architecture on the thermoelectric properties of Ag-doped $Bi_2S_3$†

T. Manimozhi, *[a] S. Kavirajan, [c] M. Navaneethan *[bc] and A. Joseph Sagaya Kennedy[d]

Received 18th June 2024
Accepted 4th November 2024

DOI: 10.1039/d4ra04467c

rsc.li/rsc-advances

Powder samples of $Bi_2S_3$ and Ag-doped $Bi_2S_3$ compounds were successfully synthesized *via* the solvothermal method. The synthesized powders were consolidated using the cold-press method and annealed at 300 °C for 3 h. The cross-sections of the consolidated samples exhibited a densely packed hierarchical architecture micro-flower-like morphology. The effect of Ag doping on the thermoelectric properties of the samples was systematically studied. The results showed that Ag doping had considerable effects on the morphology, leading to grain boundary scattering and point defects. The addition of 0.025% Ag led to an 81% enhancement in electrical conductivity ($\sigma$) at 550 K. However, a reduction in the Seebeck coefficient ($S$) was observed, and the power factor ($S^2\sigma$) was enhanced. Owing to the scattering of all-scale phonons caused by the hierarchical architecture, a low thermal conductivity of 0.407 W $m^{-1}$ $K^{-1}$ at 483 K was obtained, which is one of the low values among the reported $Bi_2S_3$ materials. The maximum $zT$ was obtained as 0.06 at 543 K for the 0.025% Ag-doped $Bi_2S_3$ sample.



## 1. Introduction

Over the past few decades, rapid progress in developing numerous thermoelectric materials has been witnessed for waste heat recovery and solid-state cooling. Thermoelectric materials have recently triggered the demonstration of excellent performance in energy conversion, without releasing any hazardous by-products in the environment. The energy efficiency of thermoelectric materials is determined using the dimensionless figure of merit ($zT$), which is defined as $zT = (\sigma S^2 T)/(\kappa_e + \kappa_l)$, where $\sigma$, $S$, $T$, $\kappa_e$ and $\kappa_l$ denote electrical conductivity (S $m^{-1}$), Seebeck coefficient (μV $K^{-1}$), absolute temperature (K), and electronic and thermal conductivity of the lattice (W $m^{-1}$ $K^{-1}$), respectively.[1] The $zT$ value has been enhanced using many strategies. In general, the reduction of lattice thermal conductivity is achieved through all scale hierarchical architecturing[2] and grain boundary phonon scattering.[3] Optimization of the power factor has been accomplished through doping,[4–6] band structure convergence,[7] quantum confinement,[8] formation of resonant states,[9] carrier energy filtering[10] and minority carrier blocking.[11]

Thermoelectricity (TE) has witnessed major achievements over the years; however, it is still a major challenge to realize synergistic optimization of lattice thermal conductivity and the power factor because of the strong coupling between these fundamental parameters. Excellent TE characteristics are displayed by materials based on $Bi_2Te_3$ (ref. 12 and 13) and PbTe[14,15] at room temperature and medium temperature, respectively. Their cost-prohibitive and highly toxic compositions, however, restrict their potential large-scale usage. Owing to its high Seebeck coefficient and low lattice thermal conductivity, bismuth sulphide ($Bi_2S_3$) is a thermoelectric compound with significant research value at moderate temperatures. In contrast to the related compound $Bi_2Te_3$, it is less toxic, more affordable, and more environmentally friendly. $Bi_2S_3$, however, has very poor electrical conductivity, which limits its commercial use.

$Bi_2S_3$ is a good semiconducting material with a direct bandgap of 1.3 eV. To date, enormous efforts have been devoted to the structural modification of $Bi_2S_3$ to enhance its thermoelectric properties. For example, the electrical resistivity of $Bi_2S_3$ was reduced by 3 orders of magnitude by introducing sulfur vacancies in the lattice positions.[16] Cui *et al.*[17] reported a reduction of the thermal conductivity together with a high $zT$

[a]*Department of Physics, Saveetha School of Engineering, Saveetha Institute of Medical and Technical Sciences (SIMATS), Saveetha University, Thandalam, Chennai-602105, India. E-mail: manimozhiavc@gmail.com*

[b]*Nanotechnology Research Centre (NRC), SRM Institute of Science and Technology, Kattankulathur, 603203, Tamil Nadu, India. E-mail: m.navaneethan@gmail.com*

[c]*Functional Materials and Energy Devices Laboratory, Department of Physics and Nanotechnology, SRM Institute of Science and Technology, Kattankulathur, 603203, Tamil Nadu, India*

[d]*Department of Physics, SRM TRP Engineering College (SRM Group), Irungalur, Tiruchirappalli-621105, Tamil Nadu, India*

† Electronic supplementary information (ESI) available. See DOI: https://doi.org/10.1039/d4ra04467c

value for Ag-doped in a Bi–Te alloy, which showed a 30% thermoelectric improvement compared with the undoped alloy. Also, the doping of Ag in the Bi sites in $Bi_2Se_3$ enhanced the $zT$ value due to the increment in the mobility and carrier concentration of free electrons. In this context, Ag has a $5s^1$ electron configuration in the outer orbital while Bi has a $6p^3$ electron. $Bi_2S_3$ and $Bi_2Se_3$ have similar structures. Hence, the doping of Ag in Bi–S based alloys could be expected to increase the structural defects. Recently, suitable element doping and a hierarchically organized microstructure morphology have been employed to enhance the $zT$ value and low thermal conductivity of thermoelectric materials. For example, Sun *et al.*[18] reported that doping $Mn^{2+}$ in the $Sb^{3+}$ sublattice increased the carrier concentration, together with a reduction in lattice thermal conductivity, which resulted in a high $zT$ value ($AgSb_{0.96}Mn_{0.04}Se_2$) of ~1.05 at 673 K. Wang *et al.*[19] reported that Ag doping and embedding a Pt quantum dot in $Mn_{0.990}Ag_{0.010}Si_{1.8}$ led to it exhibiting a higher $zT$ value (52% increase at 823 K) due to decoupling the modulation between the electrical and thermal transport properties. Zhou *et al.*[20] reported self-assembled 3D flower-like hierarchical Ti-doped $Cu_3SbSe_4$ microspheres that demonstrated a low lattice thermal conductivity of 0.38 W $m^{-1}$ $K^{-1}$ at 623 K ($Cu_3Sb_{0.93}Ti_{0.07}Se_4$) and a high $zT$ value of ~0.59 at 623 K ($Cu_3Sb_{0.96}Ti_{0.04}Se_4$). All-scale hierarchical architectures represent a potential strategy to significantly decrease $\kappa_{total}$ to reach the minimum theoretical limit,[21] but it is important that the power factor is not appreciably compromised.[22] Hence, the intellectual challenge for next-generation thermoelectric materials is to synthesize hierarchically organized microstructures[20] without compromising the power factor.

Herein, we prepared hierarchically organized architectures of $Bi_2S_3$ and Ag-doped $Bi_2S_3$ by a solvothermal method. The fundamental and functional properties of the prepared compounds were studied by various analytical techniques. It was found that the hierarchical structure could reduce the thermal conductivity. The electrical conductivity was enhanced due to the Ag doping. Hence, Ag-doped $Bi_2S_3$ provides an alternative pathway to develop toxic-free thermoelectric materials with high performance.

## 2. Experimental section

### 2.1 Synthesis procedure

All the chemicals were analytical-grade reagents and were purchased from SISCO Research Laboratories Pvt. Ltd. (SRL), India. Bismuth(III) nitrate pentahydrate ($Bi(NO_3)_3 \cdot 5H_2O$), polyethylene glycol (PEG, MW = 20 000), ethylene glycol ($C_2H_6O_2$ – EG), and thiourea ($CH_4N_2S$) were used as reagents without further purification. In accordance with the synthesis procedures outlined by Manimozhi *et al.*[23] and Dechong *et al.*,[24] we utilized PEG in our method for both size control and growth regulation. These references support our approach for optimizing the synthesis process. First, 0.01 mol of $Bi(NO_3)_3 \cdot 5H_2O$ and 2 g of PEG were dissolved in 30 mL EG, and the solution was left to stand at room temperature for 3 h without disturbance. Afterwards, 0.02 mol of thiourea was added to the above solution and stirred for a few minutes until uniform dissolution of the precursor was observed. The precursor was then hydrothermally treated in a Teflon-lined autoclave at 180 °C for 20 h. Next, centrifugation was performed using DI water and ethanol. Finally, black precipitates were obtained following drying at 80 °C, and the sample was denoted as S1. Similarly, 0.0002 mol (0.01%) and 0.0005 mol (0.025%) of $Ag(NO_3)$ was added with 0.0098 mol and 0.0095 mol of $Bi(NO_3)_3 \cdot 5H_2O$, PEG to prepare the Ag-substituted samples, which were denoted as S2 and S3.

### 2.2 Characterization

The crystalline phases and structures were examined by XRD using a Malvern PANalytical, MAERIS high-resolution benchtop X-ray diffraction system with $CuK_\alpha$ radiation ($\lambda$ = 1.5406 Å) at a scanning speed of 0.18° per minute and in the scanning angle range from 10° to 60°. The optical reflectance of the samples was obtained from the UV-Vis spectra using a 3600 PLUS: UV-Vis-NIR spectrometer equipped with an integrating sphere. $BaSO_4$ was used as the 100% reflectance standard. X-Ray photoelectron spectroscopy (XPS) was also performed using a ULVAC-PHI, Inc. spectrometer (PH15000), with an Al-$K_\alpha$ radiation source with an excitation energy of 1486.6 eV. Cross-sectional micrographs and their elemental mappings were obtained by EDS analysis of pellet samples using a high-resolution scanning electron microscopy (HR-SEM) system.

### 2.3 Thermoelectric measurements

The powder samples were pressed into pellets using a metal die of 13 mm diameter under 50 MPa pressure. The relative density of the samples was ~81% of the theoretical density (6.78 g $cm^{-3}$) of $Bi_2S_3$.[25] The samples were annealed at 300 °C in a tubular furnace in an Ar gas atmosphere for 3 h and then naturally cooled to room temperature. The total thermal conductivity ($\kappa_{total}$) of the bulk samples was measured from the relation: $\kappa_{total} = DC_p\rho$, where $D$ is the thermal diffusivity, $\rho$ is the density, and $C_p$ is the specific heat capacity of the sample. The specific heat capacity ($C_p$) was indirectly taken using Pyroceram 9606 as a reference sample in the temperature range from 303 K to 543 K and the thermal diffusivity ($D$) measurements were carried out using the laser flash method (Netzsch, LFA467HT). The density of the samples ($\rho$) was measured by Archimedes' method. The Seebeck coefficient and electrical resistivity were measured using a Seebeck coefficient/electric resistance measuring system (ZEM-3, Advance RIKO) under a He atmosphere.

## 3. Results and discussion

### 3.1 Phase structural analysis by XRD and XPS

Fig. 1a shows the XRD patterns of the powder samples while Fig. 1b shows the XRD patterns of the cold-pressed pellet samples, exhibiting the formation of the orthorhombic phase of $Bi_2S_3$, which well-matched the standard JCPDS card no: 06-0333. Compared to the pure sample (S1), the peak intensity ratio of the dominant planes of the 0.025% Ag-substituted sample (S3) was decreased and slightly shifted to the lower angle side. This

 

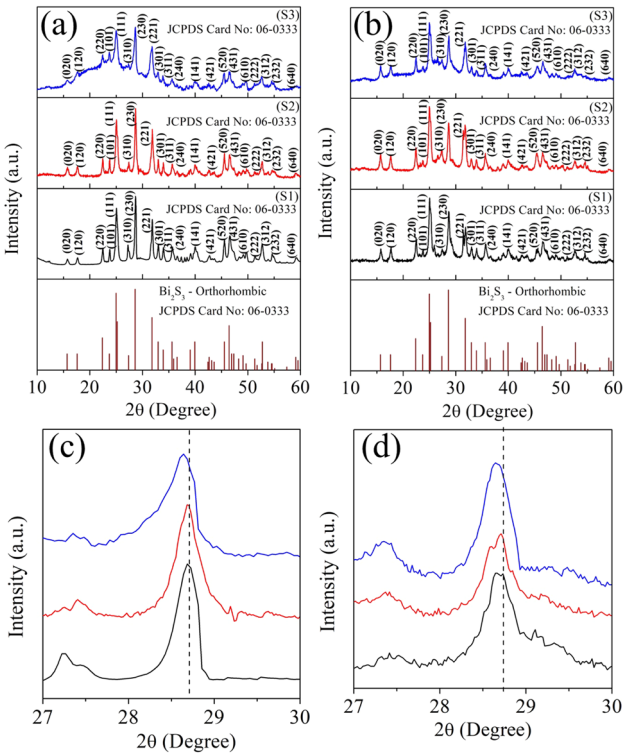


Fig. 1 XRD patterns of the samples S1 ($Bi_2S_3$), S2 (0.01% Ag-doped $Bi_2S_3$), and S3 (0.025% Ag-doped $Bi_2S_3$) (a and c) for the as-synthesized powders; (b and d) for pellets.

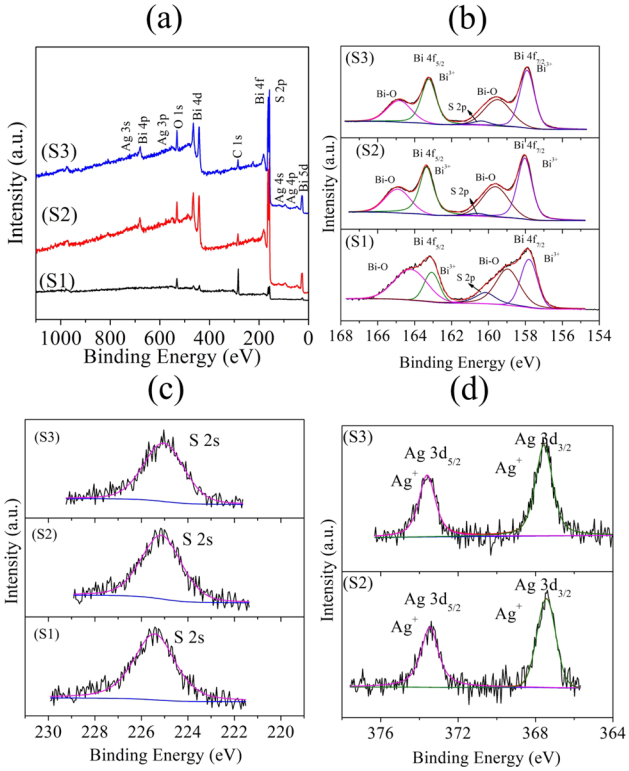


Fig. 2 XPS spectra of the samples S1 ($Bi_2S_3$), S2 (0.01% Ag-doped $Bi_2S_3$), and S3 (0.025% Ag-doped $Bi_2S_3$): (a) survey spectra; core level spectra of (b) Bi 4f, (c) S 2s, and (d) Ag 3d.

was due to the doping of Ag ions into the $Bi_2S_3$ matrix, which affected the growth orientation. In the case of the other Ag-doped sample (S2), there was a slight peak shift to the lower angle side without disturbing the peak intensity. For example, the diffraction peak for the (2 3 0) plane appeared at 28.68°, and it was shifted to a lower diffraction angle due to the incorporation of the larger ionic radius Ag ion ($Ag^+ = 115$ pm) in the $Bi^{3+}$ (96 pm) matrix. Fig. 1c and d display the corresponding (2 3 0) peak with a noticeable lower angle shift, indicating the enlargement of the unit cell size. The unit cell parameters were calculated from the diffraction peaks, and the cell parameters are listed in Table 1, which confirmed the slight enlargement in the cell parameters value for the S2 sample compared to the pure sample S1.

Table 1 Estimated values of lattice parameters for the powder samples S1, S2 and S3

| | Lattice parameters | | |
|---|---|---|---|
| Sample code | $a$ (Å) | $b$ (Å) | $c$ (Å) |
| S1 (powder) | 11.160 | 11.249 | 3.976 |
| S2 (powder) | 11.160 | 11.253 | 3.978 |
| S3 (powder) | 11.160 | 11.261 | 3.978 |
| S1 (bulk) | 11.129 | 11.241 | 3.978 |
| S2 (bulk) | 11.232 | 11.248 | 3.980 |
| S3 (bulk) | 11.299 | 11.257 | 3.987 |

X-Ray photoelectron spectroscopy (XPS) was performed to elucidate the chemical states of the elements in $Bi_2S_3$ (S1) and the 0.01% and 0.025% Ag-doped $Bi_2S_3$ (S2) and (S3) samples. The survey spectra of the samples suggested the presence of Bi, Ag, S, C, and O (Fig. 2a). In the core level Bi 4f spectra (Fig. 2b), peaks were observed at 157.80 and 163.06 eV for S1; 158.85 and 163.10 eV for S2; and 157.90 and 163.20 eV for S3 due to the spin–orbit splitting of Bi $4f_{5/2}$ and Bi $4f_{7/2}$, respectively, confirming the $Bi^{3+}$ oxidation state.[26] The interaction of the surface oxygen with the sample (Bi–O) was also observed by the peaks at the higher binding energy side. Additionally, peaks were obtained at 160.15 eV (S1), 160.28 eV (S2), and 160.37 eV (S3) correlated to the binding energies of S 2p.[26] Fig. 2c shows the binding energies of S 2 s with peaks located at 225.60 eV for S1, 225.16 eV for S2, and 225.08 eV for S3.[27] In the core level spectra of Ag 3d (Fig. 2d), peaks appeared at binding energies of 367.54 and 373.65 eV for S2; and at 367.4 and 373.4 eV for S3. These peaks were associated with Ag $3d_{5/2}$ and Ag $3d_{3/2}$, confirming the oxidation state of $Ag^+$.[27] The XPS results suggested the occurrence of a chemical shift by the changes in the corresponding binding energies for Bi 4f in S 2s and S 2p, respectively. This was due to the lower electronegativity of Ag (1.93, according to Pauling's scale) than Bi (2.02), which thus modified the electron density around the Bi ions.

### 3.2 Optical bandgap by UV-Vis-NIR analysis

Fig. 3 presents the optical bandgaps determined for the S1, S2, and S3 samples from the UV-Vis absorption spectra. These were

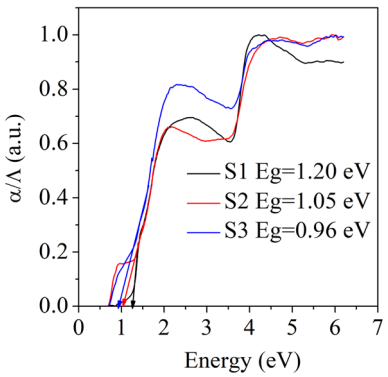


Fig. 3 Optical bandgaps of the samples S1 ($Bi_2S_3$), S2 (0.01% Ag-doped $Bi_2S_3$), and S3 (0.025% Ag-doped $Bi_2S_3$).

calculated using Kubelka–Munk's equation,[28] $\alpha/\Lambda = (1 - R)^2/(2R)$, where $R$ is the reflectance, $\alpha$ is the absorption and $\Lambda$ is the scattering coefficient, respectively. The optical bandgaps of the samples were at 1.20 eV for S1 1.05 eV for S2, and 0.96 eV for S3. The bandgap of the $Bi_2S_3$ sample (S1) matched with the reported value of 1.29 eV.[29] The decrement in the optical band gaps of samples S2 and S3 was due to the Ag doping, which may have introduced an impurity level in $Bi_2S_3$.

### 3.3 Morphological analysis by HR-SEM

Fig. 4 shows the HR-SEM micrographs and elemental mapping of the fractured surfaces of the cold-pressed bulk samples. The samples had organized hierarchical microstructures with pores. The number of pores in S1 was higher than in S2 and S3. It was observed that Ag doping suppressed the growth of the internal pores, as shown in Fig. 4a. The elemental mapping of the cross-sectional pellet samples clearly showed the uniformly distributed elements of Bi and S for the S1 sample as well as the distributions of Bi, S, and Ag for the S2 and S3 samples (Fig. 4b). The elemental compositions and spectra of the $Bi_2S_3$ (S1), 0.01% Ag-doped $Bi_2S_3$ (S2), and 0.025% Ag-doped $Bi_2S_3$ (S3) samples based on EDS analysis are outlined in Table ES1 and Fig. ES1.†

### 3.4 Thermoelectric properties

Fig. 5a shows the experimental data for the Seebeck coefficient as a function of the temperature, for which negative values were

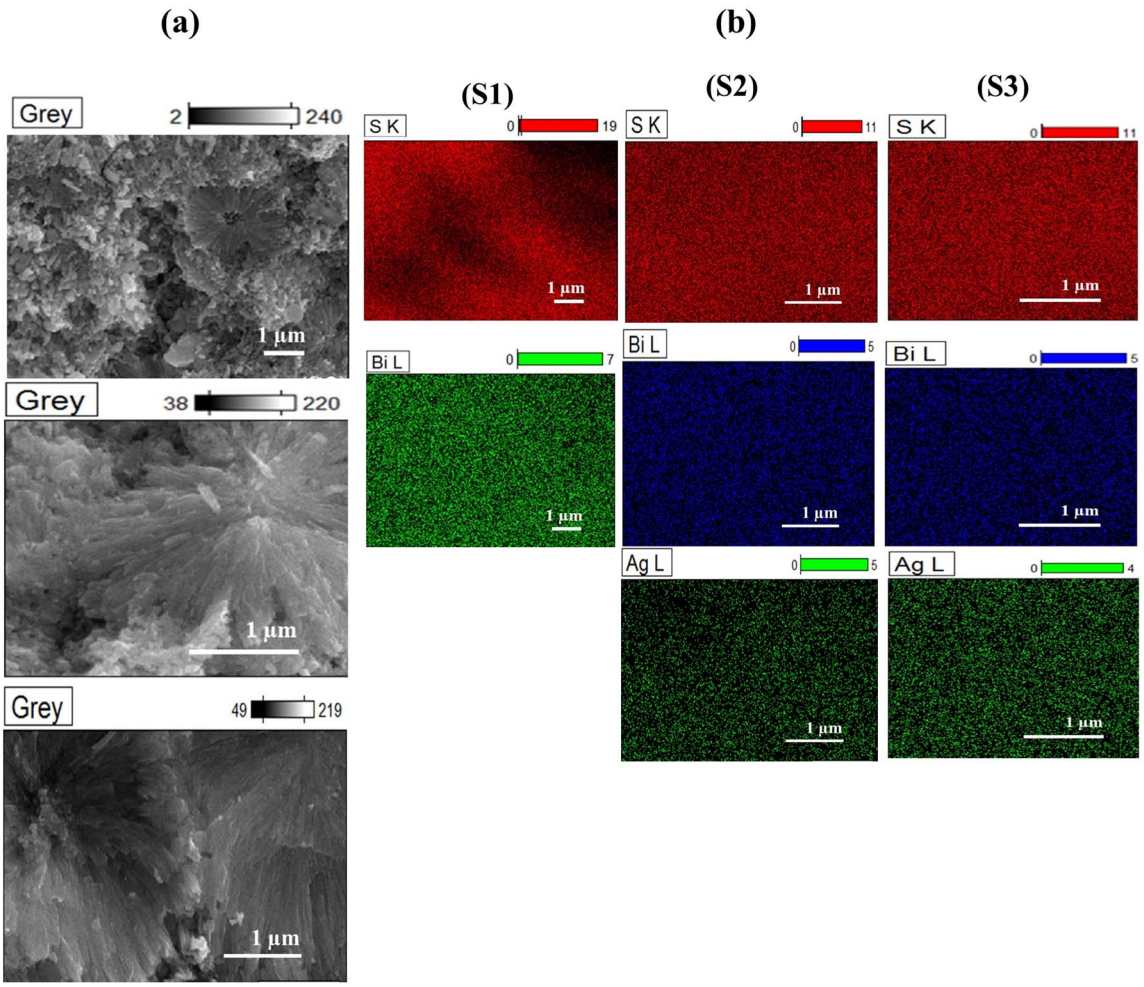


Fig. 4 (a) HR-SEM micrographs and (b) elemental mapping for cross-sectional views of the pellet samples S1 ($Bi_2S_3$), S2 (0.01% Ag-doped $Bi_2S_3$), and S3 (0.025% Ag-doped $Bi_2S_3$).

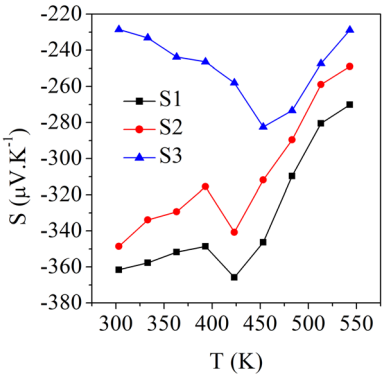


Fig. 5 Seebeck coefficient as a function of temperature for the samples S1 ($Bi_2S_3$), S2 (0.01% Ag-doped $Bi_2S_3$), and S3 (0.025% Ag-doped $Bi_2S_3$).

observed, indicating that the majority of the charge carriers were electrons (n-type behaviour). For the sample S1 ($Bi_2S_3$), the values decreased from 362 μV $K^{-1}$ at 303 K to 270 μV $K^{-1}$ at 543 K. In the case of sample S2, the values decreased from 348 μV $K^{-1}$ at 303 K to 246 μV $K^{-1}$ at 543 K. In contrast, for sample S3, the room temperature value (228 μV $K^{-1}$ at 303 K) increased to 282 μV $K^{-1}$ at 453 K and then decreased back to 228 μV $K^{-1}$ at 543 K. The maximum Seebeck coefficient was obtained as 366 μV $K^{-1}$ at 423 K for the S1 sample. Generally, the Seebeck coefficient is directly proportional to the atomic scattering factor and inversely proportional to the carrier concentration.[30] The increase–decrease phenomenon of the Seebeck coefficient was attributed to minor thermal and structural fluctuations in the samples, as indicated by the TG-DTA analysis (Fig. ES2†), which showed there were no significant structural changes. These fluctuations were observed at 423 K for S1 ($Bi_2S_3$) and at

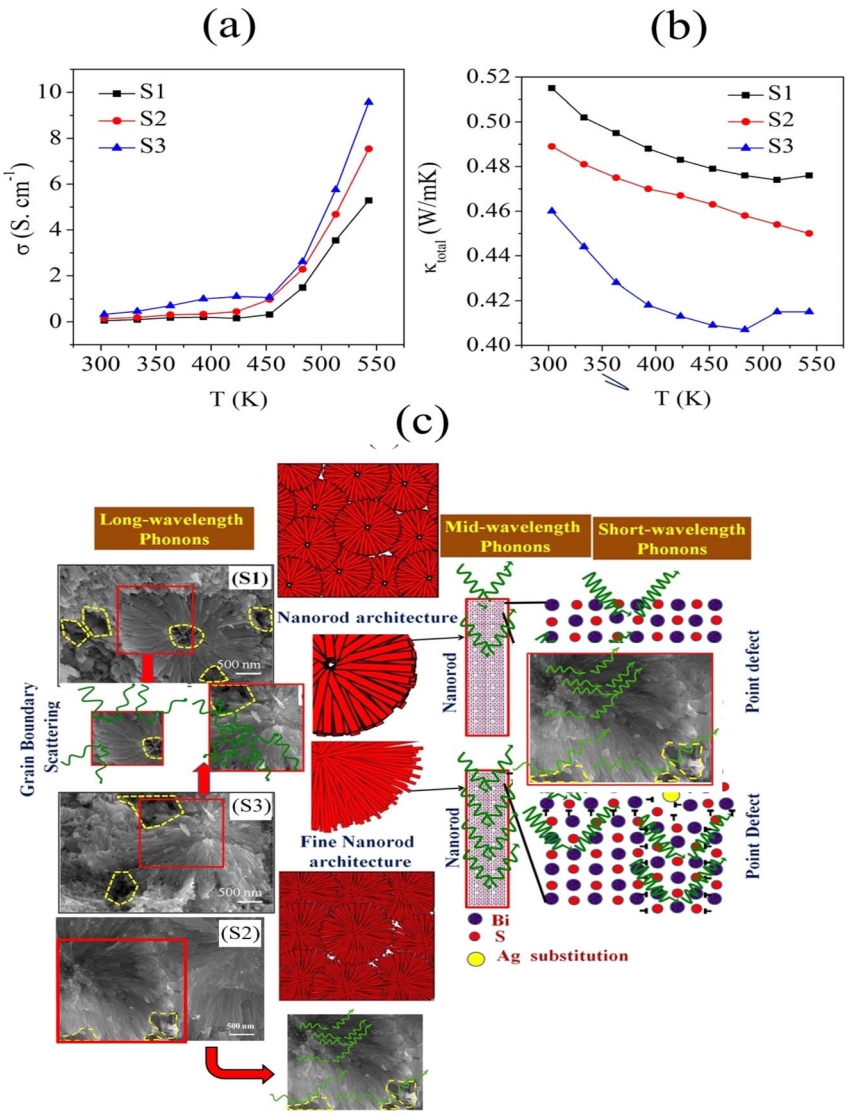


Fig. 6 (a) Temperature-dependent electrical conductivity, and (b) temperature-dependent total thermal conductivity of the samples S1 ($Bi_2S_3$), S2 (0.01% Ag-doped $Bi_2S_3$), and S3 (0.025% Ag-doped $Bi_2S_3$). (c) Schematic of the phonon scattering mechanism of the hierarchical architectures of $Bi_2S_3$ (S1), 0.01% Ag-doped $Bi_2S_3$ (S2), and 0.025% Ag-doped $Bi_2S_3$ (S3).

453 K for both S2 (0.01% Ag-doped $Bi_2S_3$) and S3 (0.025% Ag-doped $Bi_2S_3$). This behaviour may be linked to lattice distortions or a slight thermal expansion.[31]

Fig. 6a shows the electrical conductivity ($\sigma$) plots of the S1, S2, and S3 samples with the temperature ranging from 300 to 550 K, showing $\sigma$ increased from 0.054 to 5.287 S cm$^{-1}$, 0.138 to 7.537 S cm$^{-1}$, and 0.325 to 9.571 S cm$^{-1}$ for samples S1, S2, and S3, respectively. This tendency for an increase in electrical conductivity with increasing temperature was due to the semiconductor behaviour.[32] Sample S3 (0.025% Ag-doped $Bi_2S_3$) showed enhanced electrical conductivity compared to S1 and S2, due to the concentration of higher Ag-doping and the presence of a hierarchical structure and pores, which was consistent with reports.[33,34] Also, the enhancement of the electrical conductivity was attributed to the reduced bandgap, which was consistent with the UV-Vis results. Furthermore, it was also attributed to the Ag doping, which affects the electronic structure and charge carrier density.

Generally, the electrical conductivity ($\sigma$) is directly proportional to the carrier concentration ($n$) and mobility ($\mu$), and can be obtained from the expression $\sigma = ne\mu$. In samples S2 and S3, the addition of Ag (0.01% for S2 and 0.025% for S3) in interstitial sites of the $Bi_2S_3$ matrix led to an enhancement of its electrical conductivity. In n-type Ag-doped $Bi_2S_3$ materials, the electrons are majority carriers. Due to the increment in carrier concentration and decrement in mobility (Table 2), electrical conductivity enhancements were observed for the Ag-doped samples. A similar behaviour was also observed in a previous report.[35]

Fig. 6b shows the total thermal conductivity ($\kappa_{total}$) as a function of temperature for the samples. At 303 K, the $\kappa_{total}$ value was measured as 0.515 W m$^{-1}$ K$^{-1}$ for S1, 0.489 W m$^{-1}$ K$^{-1}$ for S2, and 0.46 W m$^{-1}$ K$^{-1}$ for S3. When increasing the temperature to 543 K, the values were reduced for the samples due to the strong phonon scattering, reducing to 0.476 W m$^{-1}$ K$^{-1}$ for S1, 0.45 W m$^{-1}$ K$^{-1}$ for S2, and 0.415 W m$^{-1}$ K$^{-1}$ for S3. The strong phonon scattering occurred due to the presence of a large number of grain boundaries and the edges of randomly distributed pores in the organized hierarchical microstructures. The present values of the thermal conductivity for samples S1, S2, and S3 showed low thermal conductivity values compared with the reported values, as indicated in Table 3.

Fig. 6c shows a schematic of phonon scattering in $Bi_2S_3$ (S1) 0.01% Ag-doped $Bi_2S_3$ (S2) and 0.025% Ag-doped $Bi_2S_3$ (S3). The greater number of grain boundaries, nanoscale, and point defects in the Ag-doped samples increased the number of phonon scattering centres, which reduced the thermal conductivity. Here, the Ag dopants can induce the mass contrast and lattice strain, which can significantly restrict the short-wavelength phonon transmission, leading to point defects at

Table 2 Hall measurements for the carrier concentration and mobility of samples S1–S3

| Sample code | Conduction | Carrier concentration (cm$^{-3}$) | Mobility (cm$^{-2}$ V$^{-1}$ s$^{-1}$) |
|---|---|---|---|
| S1 | n-type | $-1.09 \times 10^{18}$ | 18 |
| S2 | n-type | $-1.15 \times 10^{18}$ | 9 |
| S3 | n-type | $-1.21 \times 10^{18}$ | 1.5 |

Table 3 Comparison of the thermal conductivity in the present study with that reported in the literature

| Materials | $\kappa_{total}$ W m$^{-1}$ K$^{-1}$ | Temperature (K) | Material preparation | Pellet preparation | Morphology | References |
|---|---|---|---|---|---|---|
| $Bi_2S_3$ | ~0.77–0.59 | 303–624 K | Solid-state reaction | Spark plasma sintering | Grain sizes of 100–200 nm with dense structure | 25 |
| $Bi_2S_3$ | 0.74–0.56 | 303–573 K | Mechanical alloying | Spark plasma sintering | Dense microstructure with grain sizes of 200–300 nm | 36 |
| $Bi_2S_3$ | ~0.62–0.42 | 303–657 K | Mechanical alloying | Spark plasma sintering | Average grain size of <500 nm | 37 |
| $Bi_2S_3$ | ~0.83–0.48 | 723 K | Vacuum sealing | Spark plasma sintering | Lamellar structure with a layer stacking thickness of less than 5 μm | 38 |
| Ag-doped $Bi_2S_3$ | ~0.95–0.52 | 300–750 K | Solid-state reaction similar methods | Spark plasma sintering | Dense structure with optimal grain sizes | 39 |
| $Bi_2S_3$ | 0.515–0.473 | 303–573 K | Solvothermal | Cold-press + annealing | Dense hierarchical architecture with porous nature | PW (S1) |
| 0.01% Ag-doped $Bi_2S_3$ | 0.489–0.45 | 303–573 K | Solvothermal | Cold-press + annealing | Dense hierarchical architecture with porous nature | PW (S2) |
| 0.025% Ag-doped $Bi_2S_3$ | 0.499–0.407 | 303–573 K | Solvothermal | Cold-press + annealing | Dense hierarchical architecture with porous nature | PW (S3) |

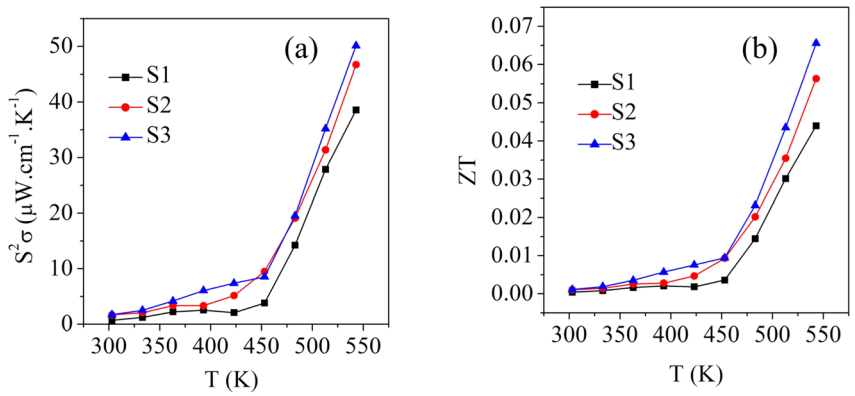


Fig. 7 Temperature dependence of the (a) power factor and (b) $zT$ values of the samples S1 ($Bi_2S_3$), S2 (0.01% Ag-doped $Bi_2S_3$), and S3 (0.025% Ag-doped $Bi_2S_3$).

the atomic scale. The nanorods sized around 100 nm can be the scattering sources of medium-wavelength phonons. So, the total thermal conductivity of sample S3 was induced by the large degree of phonon scattering due to lattice vibration. The mesoscale grain boundaries were correlated to the scattering centres of long-wavelength phonons (typically >100 nm). Due to the scattering of the all-scale phonons, including (i) short-wavelength phonon scattering due to point defects (ii) mid-wavelength phonon scattering due to mesoscale nanorods (iii) long-wavelength phonon scattering due to grain boundaries, the total thermal conductivity was greatly reduced for the S3 sample.

Fig. 7a shows the temperature dependence of the power factor ($S^2\sigma$) for the S1, S2, and S3 samples. The power factor of sample S1 was 0.7 μW cm$^{-1}$ K$^{-2}$ at 303 K and increased to 38.5 μW mK$^{-2}$ at 543 K. For the S2 sample, it was 1.67 μW cm$^{-1}$ K$^{-2}$ at 303 K and increased to 46.6 μW mK$^{-2}$ at 543 K. In contrast, S3 had a power factor of 1.7 μW cm$^{-1}$ K$^{-2}$ at 303 K, which increased to 50.1 μW mK$^{-2}$ at 543 K. The trend of the power factor followed the trend of the electrical conductivity. This was due to the greater contribution of electrical conductivity compared to the Seebeck coefficient.

Fig. 7b shows the temperature-dependent figure-of-merit ($zT$) values for all the samples. It could be clearly seen that the $zT$ value for the $Bi_2S_3$ sample (S1) increased from 0.0004–0.04 in the temperature range from 303 K to 543 K. With the addition of 0.01% Ag-doping, sample S2 showed $zT$ values of 0.001–0.056 at 303–543 K, while the 0.025% Ag-doped sample S3 showed $zT$ values of 0.001–0.06 at 303–543 K. Compared to the pure sample (S1), the 0.025% Ag-doped sample (S3) showed enhanced $zT$ values with increasing the temperature due to its enhanced power factor (Fig. 7a) and low thermal conductivity (Fig. 6b).

## 4. Conclusion

In the present study, n-type $Bi_2S_3$ and Ag-doped $Bi_2S_3$ hierarchical nanostructures were synthesized by the solvothermal method and their thermoelectric properties were investigated. It was found that Ag doping had significant effects on the morphology and the thermoelectric properties of the doped $Bi_2S_3$. The bandgap of the Ag-doped $Bi_2S_3$ sample decreased whereas the electrical conductivity and power factor increased with increasing the Ag doping due to the increment in carrier concentration. Additionally, the thermal conductivity was reduced due to the intensive scattering of phonons by the all-scale hierarchical architecture. The mass fluctuations created by Ag doping increased the scattering of phonons, which resulted in the low thermal conductivity. In particular, the 0.025% Ag-doped $Bi_2S_3$ demonstrated a good thermoelectric performance, with a low thermal conductivity of 0.415 W m$^{-1}$ K$^{-1}$ and high-power factor of 50.1 μW mK$^{-2}$ 543 K. Hence, the Ag doping of $Bi_2S_3$ along with ensuring a hierarchical architecture morphology is an effective approach to achieve a high thermoelectric performance.

## Data availability

All data underlying the results are available as part of the article, and no additional source data are required.

## Conflicts of interest

There are no conflicts to declare.

## References

1 K. Nielsch, J. Bachmann, J. Kimling and H. Böttner, Thermoelectric nanostructures: from physical model systems towards nanograined composites, *Adv. Energy Mater.*, 2011, **1**(5), 713–731, DOI: 10.1002/aenm.201100207.
2 X. Yan, Y. Feng, L. Qiu and X. Zhang, Thermal conductivity and phase change characteristics of hierarchical porous diamond/erythritol composite phase change materials, *Energy*, 2021, **233**, 121158, DOI: 10.1016/j.energy.2021.121158.
3 S. Li, Z. Huang, R. Wang, C. Wang, W. Zhao, N. Yang, F. Liu, J. Luo, Y. Xiao and F. Pan, Precision grain boundary engineering in commercial $Bi2Te_{2.7}Se_{0.3}$ thermoelectric materials towards high performance, *J. Mater. Chem. A*, 2021, **9**, 11442–11449, DOI: 10.1039/D1TA01016F.

4 A. F. Ioffe, *Semiconductor Thermoelements, and Thermoelectric Cooling*, Infosearch, 1958.
5 D. J. Singh, Doping-dependent thermopower of PbTe from Boltzmann transport calculations, *Phys. Rev. B:Condens. Matter Mater. Phys.*, 2010, **81**(19), 195217, DOI: 10.1103/PhysRevB.81.195217.
6 Y. Pei, A. LaLonde, S. Iwanaga and G. J. Snyder, High thermoelectric figure of merit in heavy hole dominated PbTe, *Energy Environ. Sci.*, 2011, **4**(6), 2085–2089, DOI: 10.1039/C0EE00456A.
7 H. Deng, X. Lou, W. Lu, J. Zhang, D. Li, S. Li, Q. Zhang, X. Zhang, X. Chen, D. Zhang and Y. Zhang, High-performance eco-friendly MnTe thermoelectrics through introducing SnTe nanocrystals and manipulating band structure, *Nano Energy*, 2021, **81**, 105649, DOI: 10.1016/j.nanoen.2020.105649.
8 A. Kumar, D. Sivaprahasam and A. D. Thakur, Colossal Seebeck coefficient in Aurivillius phase-perovskite oxide composite, *J. Alloys Compd.*, 2021, **853**, 157001, DOI: 10.1016/j.jallcom.2020.157001.
9 S. Mandava, R. Basu, B. Khasimsaheb, S. Bathula, A. Singh and S. Neeleshwar, A synergistic approach to achieving the high thermoelectric performance of La-doped SnTe using resonance state and partial band convergence, *Mater. Adv.*, 2021, **2**(13), 4352–4361, DOI: 10.1039/D1MA00155H.
10 A. T. Pham, P. T. Vo, H. K. Ta, H. T. Lai, V. C. Tran, T. L. Doan, A. T. Duong, C. T. Lee, P. K. Nair, Y. A. Zulueta and T. B. Phan, Improved thermoelectric power factor achieved by energy filtering in ZnO: Mg/ZnO hetero-structures, *Thin Solid Films*, 2021, **721**, 138537, DOI: 10.1016/j.tsf.2021.138537.
11 J. Hu, B. Liu, H. Subramanyan, B. Li, J. Zhou and J. Liu, Enhanced thermoelectric properties through minority carriers blocking in nanocomposites, *J. Appl. Phys.*, 2019, **126**(9), 095107, DOI: 10.1063/1.5118981.
12 X. Yan, B. Poudel, Y. Ma, W. S. Liu, G. Joshi, H. Wang, Y. Lan, D. Wang, G. Chen and Z. F. Ren, Experimental studies on anisotropic thermoelectric properties and structures of n-type $Bi_2Te_{2.7}Se_{0.3}$, *Nano Lett.*, 2010, **10**(9), 3373–3378.
13 J. Qiu, Y. Yan, T. Luo, K. Tang, L. Yao, J. Zhang, M. Zhang, X. Su, G. Tan, H. Xie and M. G. Kanatzidis, 3D Printing of highly textured bulk thermoelectric materials: mechanically robust BiSbTe alloys with superior performance, *Energy Environ. Sci.*, 2019, **12**(10), 3106–3117.
14 M. Ohta, K. Biswas, S. H. Lo, J. He, D. Y. Chung, V. P. Dravid and M. G. Kanatzidis, Enhancement of thermoelectric figure of merit by the insertion of MgTe nanostructures in p-type PbTe doped with $Na_2Te$, *Adv. Energy Mater.*, 2012, **2**(9), 1117–1123.
15 H. J. Wu, L. D. Zhao, F. S. Zheng, D. Wu, Y. L. Pei, X. Tong, M. G. Kanatzidis and J. Q. He, Broad temperature plateau for thermoelectric figure of merit $ZT > 2$ in phase-separated $PbTe_{0.7}S_{0.3}$, *Nat. Commun.*, 2014, **5**(1), 4515.
16 H. Mizoguchi, H. Hosono, N. Ueda and H. Kawazoe, Preparation and electrical properties of $Bi_2S_3$ whiskers, *J. Appl. Phys.*, 1995, **78**(2), 1376–1378, DOI: 10.1063/1.360315.
17 J. L. Cui, W. J. Xiu, L. D. Mao, P. Z. Ying, L. Jiang and X. Qian, Thermoelectric properties of Ag-doped n-type $(Bi_2Te_3)_{0.9}$–$(Bi_{2-x}Ag_xSe_3)$ 0.1 ($x$ = 0–0.4) alloys prepared by spark plasma sintering, *J. Solid State Chem.*, 2007, **180**(3), 1158–1162, DOI: 10.1016/j.jssc.2006.12.010.
18 Y. Sun, F. Guo, H. Qin, W. Cai and J. Sui, Enhanced thermoelectric performance of $AgSbSe_2$ *via* manganese doping, *J. Alloys Compd.*, 2021, **859**, 157844, DOI: 10.1016/j.jallcom.2020.157844.
19 Q. Wang, S. Song, X. Yang, Z. Liu, Y. Ma, X. San, J. Wang, D. Zhang, S. F. Wang and Z. Li, Incorporating element doping and quantum dot embedding effects to enhance the thermoelectric properties of higher manganese silicides, *Journal of Materiomics*, 2021, **7**(2), 377–387, DOI: 10.1016/j.jmat.2020.08.008.
20 T. Zhou, L. Wang, S. Zheng, M. Hong, T. Fang, P. P. Bai, S. Chang, W. Cui, X. Shi, H. Zhao and Z. G. Chen, Self-assembled 3D flower-like hierarchical Ti-doped $Cu_3SbSe_4$ microspheres with ultralow thermal conductivity and high $zT$, *Nano Energy*, 2018, **49**, 221–229, DOI: 10.1016/j.nanoen.2018.04.035.
21 K. Biswas, J. He, I. D. Blum, C. I. Wu, T. P. Hogan, D. N. Seidman, V. P. Dravid and M. G. Kanatzidis, High-performance bulk thermoelectrics with all-scale hierarchical architectures, *Nature*, 2012, **489**(7416), 414–418, DOI: 10.1038/nature11439.
22 M. Hong, Z. G. Chen, L. Yang and J. Zou, Enhancing thermoelectric performance of $Bi_2Te_3$-based nanostructures through rational structure design, *Nanoscale*, 2016, **8**(16), 8681–8686, DOI: 10.1039/C6NR00719H.
23 T. Manimozhi, J. Archana, M. Navaneethan and K. Ramamurthi, Shape-controlled synthesis of $AgBiS_2$ nano-/microstructures using PEG-assisted facile solvothermal method and their functional properties, *Appl. Surf. Sci.*, 2019, **487**, 664–673.
24 D. Ma, S. Pan, M. Tan, G. He and J. Zhao, Shape-controlled synthesis of varied bismuth nanostructures and their size-dependent photocatalytic removal of organic dyes under visible light irradiation, *Opt. Mater.*, 2023, 114433.
25 Y. Wu, Q. Lou, Y. Qiu, J. Guo, Z. Y. Mei, X. Xu, J. Feng, J. He and Z. H. Ge, Highly enhanced thermoelectric properties of nanostructured $Bi_2S_3$ bulk materials *via* carrier modification and multi-scale phonon scattering, *Inorg. Chem. Front.*, 2019, **6**(6), 1374–1381, DOI: 10.1039/C9QI00213H.
26 A. K. Abay, D. H. Kuo, X. Chen and A. D. Saragih, A new V-doped Bi2 (O, S) 3 oxysulfide catalyst for highly efficient catalytic reduction of 2-nitroaniline and organic dyes, *Chemosphere*, 2017, **189**, 21–31, DOI: 10.1016/j.chemosphere.2017.09.018.
27 S. N. Guin and K. Biswas, Cation disorder and bond anharmonicity optimize the thermoelectric properties in kinetically stabilized rocksalt $AgBiS_2$ nanocrystals, *Chem. Mater.*, 2013, **25**(15), 3225–3231, DOI: 10.1021/cm401630d.
28 G. Tan, F. Shi, S. Hao, L. D. Zhao, H. Chi, X. Zhang, C. Uher, C. Wolverton, V. P. Dravid and M. G. Kanatzidis, Non-equilibrium processing leads to record high thermoelectric

figure of merit in PbTe–SrTe, *Nat. Commun.*, 2016, **7**(1), 12167, DOI: **10.1038/ncomms12167**.

29 Y. Q. Yu, B. P. Zhang, Z. H. Ge, P. P. Shang and Y. X. Chen, Thermoelectric properties of Ag-doped bismuth sulfide polycrystals prepared by mechanical alloying and spark plasma sintering, *Mater. Chem. Phys.*, 2011, **131**(1–2), 216–222, DOI: **10.1016/j.matchemphys.2011.09.010**.

30 G. P. Srivastava, Tuning phonon properties in thermoelectric materials, *Rep. Prog. Phys.*, 2015, **78**(2), 026501, DOI: **10.1088/0034-4885/78/2/026501**.

31 K. Łukaszewicz, J. Stępień-Damm, A. Pietraszko, A. Kajokas and J. Grigas, Crystal structure, thermal expansion, dielectric permittivity and phase transitions of $Bi_2S_3$, *Pol. J. Chem.*, 1999, **73**(3), 541–546.

32 L. Kush, S. Srivastava, Y. Jaiswal and Y. Srivastava, Thermoelectric behaviour with high lattice thermal conductivity of nickel base $Ni_2CuCrFeAl_x$ ($x = 0.5$, 1.0, 1.5 and 2.5) high entropy alloys, *Mater. Res. Express*, 2020, **7**(3), 035704.

33 E. Redel and H. Baumgart, Thermoelectric porous MOF based hybrid materials, *APL Mater.*, 2020, **8**(6), 060902, DOI: **10.1063/5.0004699**.

34 R. Jin, G. Chen and J. Pei, PbS/PbSe hollow spheres: solvothermal synthesis, growth mechanism, and thermoelectric transport property, *J. Phys. Chem. C*, 2012, **116**(30), 16207–16216, DOI: **10.1021/jp302206q**.

35 Y. Ren, Q. Jiang, J. Yang, Y. Luo, D. Zhang, Y. Cheng and Z. Zhou, Enhanced thermoelectric performance of MnTe *via* Cu doping with optimized carrier concentration, *Journal of Materiomics*, 2016, **2**(2), 172–178, DOI: **10.1016/j.jmat.2016.05.008**.

36 Z. H. Ge, B. P. Zhang, Z. X. Yu and J. F. Li, Effect of spark plasma sintering temperature on thermoelectric properties of $Bi_2S_3$ polycrystal, *J. Mater. Res.*, 2011, **26**(21), 2711–2718, DOI: **10.1557/jmr.2011.273**.

37 J. Guo, Q. Lou, Y. Qiu, Z. Y. Wang, Z. H. Ge, J. Feng and J. He, Remarkably enhanced thermoelectric properties of $Bi_2S_3$ nanocomposites *via* modulation doping and grain boundary engineering, *Appl. Surf. Sci.*, 2020, **520**, 146341, DOI: **10.1016/j.apsusc.2020.146341**.

38 J. Yan, J. Yang, B. Ge, G. Liu, Z. Shi, Z. Duan and G. Qiao, Effect of Silver and Iodine Co-doping on the Thermoelectric Properties of n-Type $Bi_2S_3$, *J. Electron. Mater.*, 2019, **48**, 503–508, DOI: **10.1007/s11664-018-6741-4**.

39 H. Hou, J. Yang, G. Liu, X. Zhang and G. Qiao, Effects of cation doping on thermoelectric properties of $Bi_2S_3$ materials, *J. Mater. Sci.: Mater. Electron.*, 2022, **33**(28), 22291–22299, DOI: **10.1039/d2xx00000h**.